# Designing artificial two-dimensional landscapes via atomic-layer substitution

Yunfan Guo[a,1,2], Yuxuan Lin[a,1], Kaichen Xie[b,1], Biao Yuan[c], Jiadi Zhu[a], Pin-Chun Shen[a], Ang-Yu Lu[a], Cong Su[d], Enzheng Shi[e,f], Kunyan Zhang[g], Changan HuangFu[h], Haowei Xu[d], Zhengyang Cai[a], Ji-Hoon Park[a], Qingqing Ji[a], Jiangtao Wang[a], Xiaochuan Dai[a], Xuezeng Tian[i], Shengxi Huang[g], Letian Dou[e], Liying Jiao[h], Ju Li[d], Yi Yu[c], Juan-Carlos Idrobo[j], Ting Cao[b], Tomás Palacios[a], and Jing Kong[a,2]

[a]Department of Electrical Engineering and Computer Science, Massachusetts Institute of Technology, Cambridge, MA 02139; [b]Department of Materials Science and Engineering, University of Washington, Seattle, WA 98195; [c]School of Physical Science and Technology, ShanghaiTech University, Shanghai 201210, China; [d]Department of Nuclear and Materials Science and Engineering, Massachusetts Institute of Technology, Cambridge, MA 02139; [e]Davidson School of Chemical Engineering, Purdue University, West Lafayette, IN 47907; [f]Key Laboratory of 3D Micro/Nano Fabrication and Characterization of Zhejiang Province, School of Engineering, Westlake University, Hangzhou 310024, China; [g]Department of Electrical Engineering, The Pennsylvania State University, University Park, PA 16802; [h]Key Laboratory of Organic Optoelectronics and Molecular Engineering of the Ministry of Education, Department of Chemistry, Tsinghua University, Beijing 100084, China; [i]Beijing National Laboratory for Condensed Matter Physics, Institute of Physics, Chinese Academy of Sciences, Beijing 100190, China; and [j]Center for Nanophase Materials Sciences, Oak Ridge National Laboratory, Oak Ridge, TN 37831.

Edited by Kin Fai Mak, Cornell University, Ithaca, NY, and accepted by Editorial Board Member Evelyn L. Hu June 23, 2021 (received for review March 30, 2021)

**Technology advancements in history have often been propelled by material innovations. In recent years, two-dimensional (2D) materials have attracted substantial interest as an ideal platform to construct atomic-level material architectures. In this work, we design a reaction pathway steered in a very different energy landscape, in contrast to typical thermal chemical vapor deposition method in high temperature, to enable room-temperature atomic-layer substitution (RT-ALS). First-principle calculations elucidate how the RT-ALS process is overall exothermic in energy and only has a small reaction barrier, facilitating the reaction to occur at room temperature. As a result, a variety of Janus monolayer transition metal dichalcogenides with vertical dipole could be universally realized. In particular, the RT-ALS strategy can be combined with lithography and flip-transfer to enable programmable in-plane multiheterostructures with different out-of-plane crystal symmetry and electric polarization. Various characterizations have confirmed the fidelity of the precise single atomic layer conversion. Our approach for designing an artificial 2D landscape at selective locations of a single layer of atoms can lead to unique electronic, photonic, and mechanical properties previously not found in nature. This opens a new paradigm for future material design, enabling structures and properties for unexplored territories.**

2D materials | Janus transition-metal dichalcogenides | atomic-layer substitution | room temperature | heterostructures

The wide and rich physics of two-dimensional (2D) materials have led to the fabrication of heterostructures (1–5), superlattices (6–8), and twisted structures (9–11) with breakthrough discoveries and applications. During the past 3 y, a new class of atomic layer structures, in which the top layer chalcogen atoms within the three-atom-thick transition-metal dichalcogenides (TMDs) are replaced by a different type of chalcogen atoms, has been developed, resulting in a Janus monolayer with broken out-of-plane symmetry, inherit strain, and a variety of attractive properties (12–16). However, such a transition has been subjected to thermal energy input because the top chalcogen–metal bonds need to be broken in order for the substitution to occur. Previous strategies (12, 15, 16) usually break off the original chalcogen atoms by purely harsh energetic means and then form new bonds with the incoming replacements. Since the displacement energies of these chalcogen atoms in 2D TMDs range from 5 to 7 eV (17, 18), the process requires either knocking off the top chalcogens via the kinetic energy of atoms in a hydrogen (12) or Se plasma (16) or purely high temperature (to form sulfur vacancies) (15) to happen.

It is well known that thermal energy has been widely used to enable chemical reactions. However, high reaction temperatures incur severe limitations (for example, the types of substrate on which materials can be synthesized) and undesirable energy consumptions. There has been a continuing pursuit to reduce material synthesis temperatures while maintaining the quality of as-synthesized material (19–21). Recently, a room-temperature method to synthesis monolayer Janus WSSe and MoSSe by sulfurization from monolayer $WSe_2$ and $MoSe_2$ was reported (14). Nevertheless, the mechanism for such conversion was only hypothesized and has not been completely understood.

This paper reports our concurrent work for room-temperature atomic-layer substitution (RT-ALS), including the conversion of $WSe_2$ and $MoSe_2$ (2H phase) being sulfurized into Janus WSeS and MoSeS, $WS_2$ and $MoS_2$ (2H phase) being selenized into Janus WSSe and MoSSe, and the conversion of 1T' $MoS_2$ being selenized into Janus 1T' MoSSe. Using density functional theory

## Significance

**Manipulating materials with atomic-scale precision is essential for the development of a next-generation material design toolbox. Tremendous efforts have been made to advance the compositional, structural, and spatial accuracy of material deposition and patterning. Here, we presented a new reaction pathway to implement the conversions of two-dimensional materials within the atomic-layer thickness at room temperature for electrical dipole manipulation. Not only could various Janus monolayer transition metal dichalcogenides with vertical dipole be realized, but also some heterostructures, including the dipole-nondipole heterostructures ($MoS_2$-MoSSe) and multiheterostructures ($MoS_2$-MoSSe-MoSeS-$MoSe_2$) within the same monolayer host structure are developed, in which the dipoles can be selectively patterned to be zero ($MoS_2$, $MoSe_2$), positive (MoSSe), and negative (MoSeS).**

Author contributions: Y.G. and J.K. designed research; Y.G., Y.L., K.X., B.Y., J.Z., P.-C.S., A.-Y.L., C.S., E.S., H.X., J.-C.I., and T.C. performed research; C.H. and L.J. contributed new reagents/analytic tools; Y.G., Y.L., K.X., B.Y., J.Z., P.-C.S., A.-Y.L., C.S., E.S., K.Z., H.X., Z.C., J.-H.P., Q.J., J.W., X.D., X.T., S.H., L.D., J.L., Y.Y., J.-C.I., T.C., and T.P. analyzed data; and Y.G., Y.L., T.C., and J.K. wrote the paper.

The authors declare no competing interest.

This article is a PNAS Direct Submission. K.F.M. is a guest editor invited by the Editorial Board.



[1]Y.G., Y.L., and K.X. contributed equally to this work.

[2]To whom correspondence may be addressed. Email: jingkong@mit.edu or yfguo112@mit.edu.

This article contains supporting information online at https://www.pnas.org/lookup/suppl/doi:10.1073/pnas.2106124118/-/DCSupplemental.

Published August 5, 2021.

(DFT) calculations, we were able to elucidate the evolution of free energies in each reaction step and present a clear understanding of why such a reaction can occur at room temperature. More significantly, by combining RT-ALS with lithography patterning and flip 2transfer, a completely new class of monolayer lateral heterostructures and multiheterostructures are designed and fabricated.

Fig. 1*A* illustrates our RT-ALS process. The presence of hydrogen radicals (22) produced by a remote plasma strip the chalcogenide atoms on the top layer in a gentle and chemical way. Meanwhile, the low-pressure system facilitates the supply of vaporized chalcogen substitutes (here illustrated with Se) to take the place of missing atoms, resulting in an asymmetric Janus structure of MXY (M = Mo or W, X = S or Se, and Y = Se or S) at room temperature.

## Results and Discussion

In sharp contrast to previous severe strategies (12, 15, 16), the RT-ALS steers the reaction via a different pathway. We use DFT (within the generalized gradient approximation, including van der Waals corrections [PBE-D2] on a supercell containing 4 $MoS_2$ unit cells [larger supercells are included in the *SI Appendix*]) to examine two reaction pathways to illustrate the difference, as shown in Fig. 1 *B–D* and *SI Appendix*, Fig. S1*D*. One pathway is the conventional high-temperature substitution (replacing S by Se via thermal activation), and the other is our RT-ALS process. Due to the active roles of H radicals in the RT-ALS process, the energy barrier becomes much lower, and the process is overall exothermic. Fig. 1*B* exhibits that H radicals firstly adsorb on the upper surface of monolayer $MoS_2$ with adsorption energy of ∼0.5 eV/H (which further increases with the H coverage, as shown in *SI Appendix*, Fig. S1*A*). As the H coverage increases, two H atoms form bonds with one S atom (*SI Appendix*, Fig. S1*B*), and the $H_2S$ desorbs, leaving an S vacancy. Surprisingly, this desorption process only involves a small activation barrier <0.5 eV (i.e., 12 kcal/mol), an order of magnitude smaller than the total bond energies of 3 Mo-S bonds (∼6 eV). In such a scenario, the removal of S is unlikely to be caused by collisions with hydrogen radicals because the kinetic energy of an H radical in the remote hydrogen plasma is about two orders of magnitude smaller than the displacement energy of a chalcogen atom (16), and the masses are very different between H and S atoms. The S vacancy is then occupied by a nearby Se atom. In contrast, the high-temperature pathway (*SI Appendix*, Fig. S1*D*) involves Se adsorption on surface, Mo-S bond breaking, and Mo-Se bond reforming, requiring an energy barrier of ∼2.5 eV that occurs when the Mo-S bond breaks (Fig. 1*D*). This calculated energy barrier matches well with the experimental findings, wherein the high-temperature substitution happens at ∼1,000 K (23). Such a calculation comparison clearly reveals that RT-ALS is made possible via reducing the reaction energy barrier, and the reaction kinetics is controlled by the active H radicals.

For RT-ALS experiments, we start with chemical vapor deposition (CVD)-synthesized monolayer $MoS_2$ and perform selenization for the top sulfur layer to obtain MoSSe. Afterward, we use flip-transfer to expose the bottom surface and perform RT-ALS a second time to achieve MoSSe conversion to $MoSe_2$ (*SI Appendix*, Fig. S2). From the optical microscopy (OM) images (*SI Appendix*, Fig. S2 *B–D*), the optical contrast of the $MoS_2$, MoSSe, and converted $MoSe_2$ triangular single crystals remain uniform and intact after RT-ALS, suggesting the process makes negligible disruption to the 2D lattice. This is also confirmed by atomic force microscopy (AFM) images (*SI Appendix*, Fig. S2 *E–G*), as their surfaces remain pristine and flat after each RT-ALS step. In addition, it is straightforward to extend the single/double-sided conversions to continuous large-area films (*SI Appendix*, Fig. S2 *H–J*). From a material synthesis perspective, here $MoSe_2$ is obtained from a $MoS_2$ template by room-temperature reaction, without the need of high-temperature conversions as in contrast to earlier approaches (21, 24), and thus avoids subsequent lattice or substrate damage. This provides an alternative route to obtain Se-based TMDs at room temperature. More importantly, this could be used to synthesize TMD materials that are hard to be directly grown by CVD or other methods.

To confirm the substitution of the top chalcogenide layer, measurements on Raman and photoluminescence (PL) spectroscopy

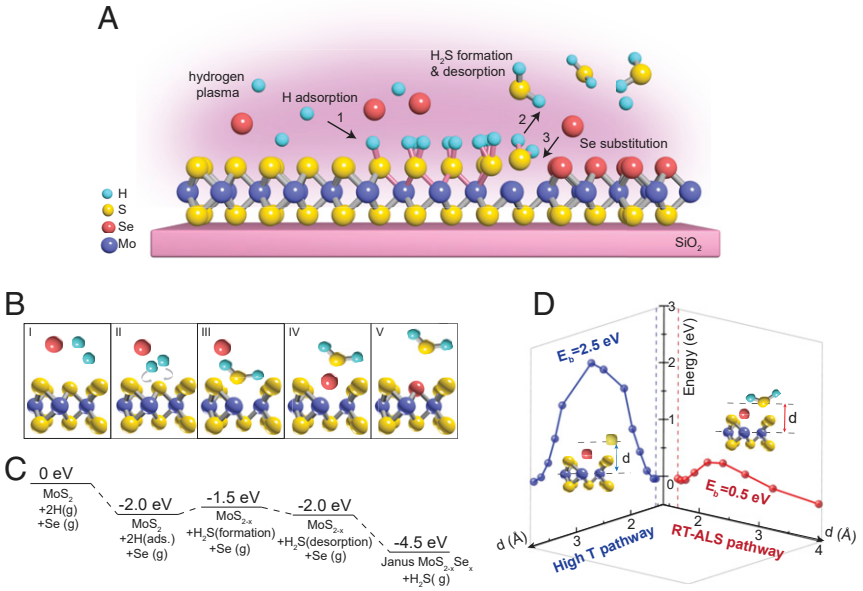


**Fig. 1.** RT-ALS with DFT calculation and comparison. (*A*) Schematic illustration of the RT-ALS process from monolayer $MoS_2$. (*B*) Schematics of the five key reaction steps for RT-ALS process (cartons from left to right): before H adsorption, 2 H adsorption and diffusion to the same S, formation of $H_2S$, desorption of $H_2S$, and Se occupation of the S vacancy. Purple, yellow, red, and green balls are Mo, S, Se, and H atoms, respectively. (*C*) Free energy of each step in *B*, relative to that of the first step. (*D*) Comparison of activation energy barrier between the RT-ALS strategy (red) and the conventional high-temperature substitution (blue). The axes of the two pathways correspond to distances (d) between the substituted S atom to Mo plane in each case. The vertical dashed lines (blue and red) indicate equilibrium S to Mo plane distances (1.54 Å for high T pathway, 1.64 Å for RT-ALS pathway). In RT-ALS process, the largest energy barrier occurs at a critical distance where $H_2S$ starts to form. In the high-temperature pathway, the largest energy barrier corresponds to when S and Se are both disconnect with Mo.

are performed due to their sensitivity to the crystal structure. For TMDs, the $A_{1g}$ and $E_{2g}$ mode correspond to the out-of-plane and in-plane lattice vibrations, respectively. Therefore, changing the top layer of chalcogens produces different phonon frequencies for the same type of lattice vibrations. As shown in Fig. 2*A*, the $MoS_2$ $A_{1g}$ (404 $cm^{-1}$) and $E_{2g}$ (383 $cm^{-1}$) modes shift to 288 $cm^{-1}$ and 355 $cm^{-1}$, respectively, in Janus MoSSe[12] due to the change of atomic mass and the broken symmetry in the vertical direction (12). Further flip-transfer and RT-ALS on the other sulfur layer yield full selenization, with a sharp peak at ~239 $cm^{-1}$ and a broad one at ~284 $cm^{-1}$, which are consistent with the $A_{1g}$ and $E_{2g}$ modes in monolayer $MoSe_2$ (25). These conversions are further evidenced by the strong PL emission shown in Fig. 2*B*, in which the PL peak energy shifts from 1.85 eV (pristine $MoS_2$) to 1.72 eV (Janus MoSSe) and then to 1.60 eV (converted $MoSe_2$). All the observed PL peak energies are consistent with reported values of previous literature (12, 25). Besides, Raman mappings (*SI Appendix*, Fig. S3 *A–C*) and PL intensity mappings (Fig. 2*B*, Insets) also confirm that crystals produced by RT-ALS have high spatial homogeneity.

This RT-ALS is found to be a general strategy to obtain various Janus materials (including different transition metal atoms, chalcogen atoms, for converting only top layer or both top and bottom layers, and different crystal phases) through our experimental investigations. The conversions from $WS_2$ to Janus WSSe and then to $WSe_2$ were successfully obtained (*SI Appendix*, Figs. S2 *K–M* and S3 *G–I*), with the corresponding PL emissions shift from 2.01 eV ($WS_2$) to 1.83 eV (WSSe) and to 1.63 eV ($WSe_2$) (Fig. 2*D*). Compared with MoSSe, the larger elastic modulus and smaller carrier effective mass of WSSe may give rise to higher carrier mobility, especially for holes, due to the stronger spin-orbit coupling and overall cleaner optical signatures of W (16, 26). In addition, the conversion from monolayer $MSe_2$ (M = Mo and W) to Janus MSeS and then to $MS_2$ are realized by sulfurization (Fig. 2*C* and *SI Appendix*, Fig. S3 *D–F*) as well as the conversion from 1T' $MoS_2$ to Janus 1T' MoSSe (*SI Appendix*, Fig. S3 *J* and *K*). The evolutions of Raman peaks are all in consistent with literature (12, 16, 27) and our theoretical predictions, suggesting the universality of RT-ALS strategy.

In order to verify the atomic structure of Janus MoSSe, we used annular dark-field scanning transmission electron microscopy (ADF-STEM) to obtain the tilted images of MoSSe. The image was obtained by rotating the MoSSe sample 10° from the [001] crystallographic orientation to a new orientation that resulted in the Mo, Se, and S atoms projected in a straight line. In that way, the Mo, Se, and S atoms can be individually identified. As shown in Fig. 2*E*, the tilted ADF-STEM image enables to separate the Se and S atoms. The results show that the Se atoms are located on one side of the monolayer MoSSe, and S atoms on the opposite side, which is direct evidence of the Janus structure. The corresponding intensity profile in Fig. 2*F* clearly show the individual Mo, Se and S atoms with their total peak intensities proportional to their atomic numbers.



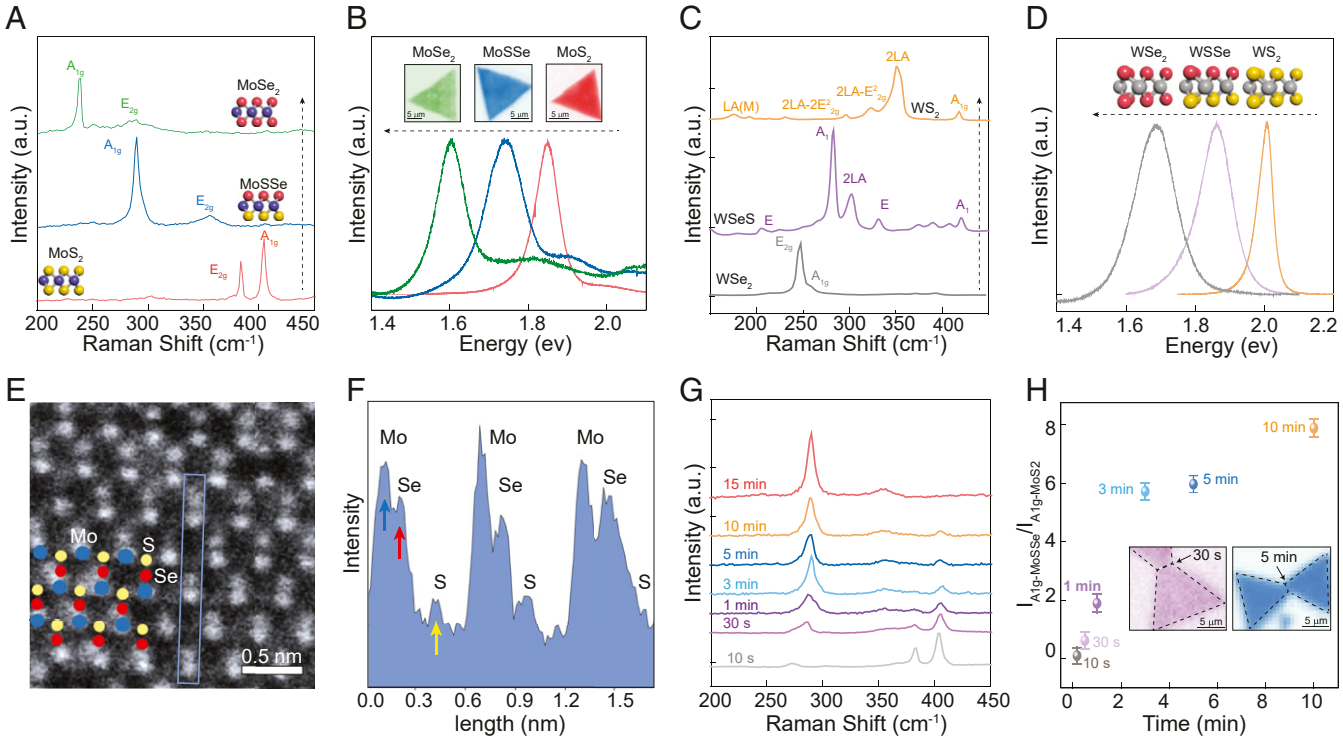


**Fig. 2.** Characterizations of the monolayer (Janus) TMDs converted using RT-ALS and the conversion process. (*A*) Raman spectra of starting monolayer $MoS_2$, Janus MoSSe, and converted $MoSe_2$. (*Insets*) Crystal structures of $MoS_2$, Janus MoSSe, and $MoSe_2$, respectively. (*B*) PL spectra of starting monolayer $MoS_2$, Janus MoSSe, and converted $MoSe_2$. (*Insets*) Spatially resolved PL mappings of $MoS_2$, Janus MoSSe, and converted $MoSe_2$ flakes at 1.85 eV, 1.72 eV, and 1.60 eV, respectively. (*C*) Raman spectra of starting monolayer $WSe_2$, Janus WSeS, and converted $WS_2$. (*D*) PL spectra of starting monolayer $WS_2$, Janus WSSe, and converted $WSe_2$. (*Insets*) Crystal structures of $WS_2$, Janus WSSe, and $WSe_2$, respectively. (*E*) Tilted ADF-STEM image of a MoSSe sample to visualize the asymmetric atom structure in the vertical direction. The corresponding Mo, Se, and S atoms are schematically shown with blue, red, and yellow circles, respectively. (*F*) Intensity profile for the atomic chain highlighted in blue in *E* shows the intensity of individual Mo, Se, and S atoms. (*G*) Raman spectra collected at several monolayer Janus MoSSe samples treated with hydrogen plasma for 10 s, 30 s, 1 min, 3 min, 5 min, 10 min, and 15 min, respectively. (*H*) The relationship between the conversion time (10 s, 30 s, 1 min, 3 min, 5 min, and 10 min, respectively) and the corresponding intensity $I_{A1g(MoSSe)}/I_{A1g(MoS2)}$ ratio over the conversion process. (*Inset*) Spatially resolved Raman mappings of two coalesced Janus MoSSe flakes converted within 30 s and 5 min, respectively, which show uniform Raman intensity over the whole MoSSe regions.

To achieve a better understanding of the conversion process, we investigated the evolution of the Raman peaks during the synthesis. The results indicated in Fig. 2 *G* and *H*, and *SI Appendix*, Fig. S4*A* show that within 10 s, the $A_{1g}$ peak of Janus MoSSe begins to emerge [at a frequency ~10 $cm^{-1}$ lower than the final point, most likely due to the modulation of phonon frequency from the local phonon vibrations at the reaction onset (26)]. The intensity of the Janus MoSSe $A_{1g}$ mode increases with longer conversion time; meanwhile, the intensity of the $MoS_2$ $A_{1g}$ peak decreases and eventually vanishes in 15 min. Based on the variation of Raman peaks at different time, the conversion yield (roughly defined by Y% = Intensity $A_{1g}$ of MoSSe/[Intensity $A_{1g}$ of MoSSe + Intensity $A_{1g}$ of $MoS_2$]) from S to Se after RT-ALS treatment are estimated (*SI Appendix*, Fig. S4*B*). For material conversion through high-temperature substitution, previous reports (21) showed that the atomic replacement begins at energetically favorable sites (crystal edges, defect sites, and grain boundaries) and gradually progresses to the other regions of the flakes, indicating it is controlled by thermodynamics. In contrast, the room temperature operation here suggests it is a kinetic process, in which the energy needed for the atomic substitution is supplied by the highly reactive hydrogen radicals. This leads to the spatially homogeneous substitution of atoms over the whole flake since the reaction onset (Fig. 2*H*, Insets and *SI Appendix*, Fig. S4*C*) and a fast progression of the reaction with a time scale as short as 30 s (Fig. 2*G* and *SI Appendix*, Fig. S4*A*).

Taking advantage of the room temperature procedure of the whole process, the programmable design in monolayer TMD can be realized using lithography combined with flip-transfer techniques, as illustrated in Fig. 3 *A*–*C*. Arbitrary patterns in a 2D plane can be implemented by using a physical mask (here, lithographic patterns is just an example), enabling locally programmed out-of-plane atomic structures (Fig. 3*A*, where electron-beam lithography [EBL] can define arbitrary patterns using a polymethyl methacrylate [PMMA] mask). RT-ALS will convert the exposed areas to MSSe, allowing the formation of lateral heterostructure between $MS_2$ and Janus

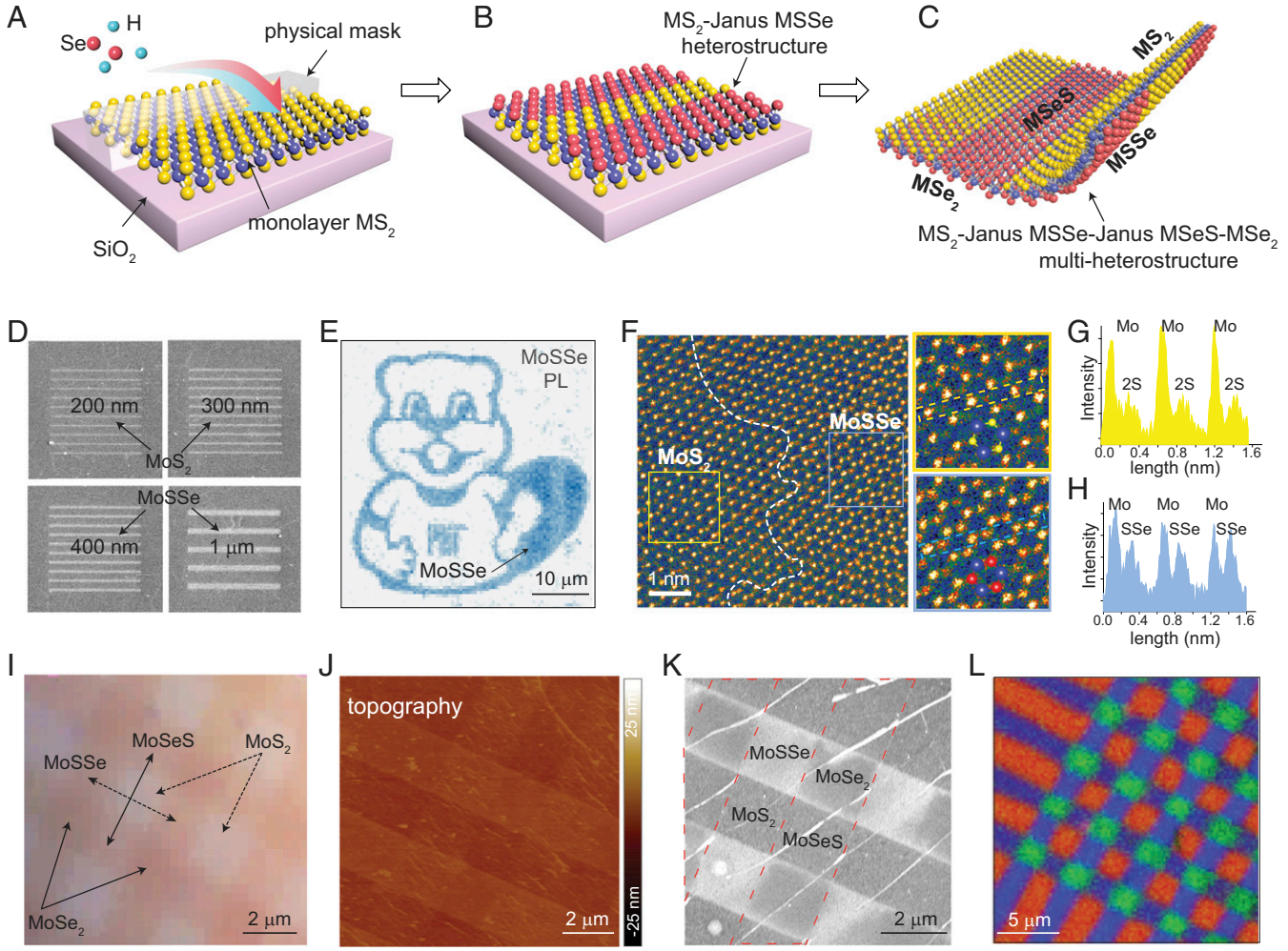


**Fig. 3.** RT-ALS with programmable design in dipole/nondipole lateral heterostructures and multiheterostructure. (*A*) Schematic representation of programmable ALS process by lithography patterning and ALS process. (*B*) Programmable monolayer $MoS_2$-Janus MoSSe heterostructure on $SiO_2$/Si substrate. (*C*) A multiheterostructure composed of monolayer $MoS_2$-Janus MoSSe-Janus MoSeS-$MoSe_2$ regions. (*D*) SEM images of monolayer Janus MoSSe-$MoS_2$ stripe patterns with different widths. (*E*) Spatially resolved PL mapping for a Massachusetts Institute of Technology mascot "Tim the beaver" pattern (Janus MoSSe) on a monolayer $MoS_2$ canvas. (*F*) Pseudocolor ADF-STEM image of a $MoS_2$-MoSSe interface (*Left*), the zoomed-in views of a $MoS_2$ region (*Right Top*, highlighted in yellow) and a Janus MoSSe region (*Right Bottom*, highlighted in blue), and their respective intensity profiles in *G* and *H*. (*I*) OM image of monolayer multijunction composed with $MoS_2$-Janus MoSSe-Janus MoSeS-$MoSe_2$. (*J*) AFM topography image for the monolayer multiheterostructure of $MoS_2$-Janus MoSSe-Janus MoSeS-$MoSe_2$. (*K*) SEM image of monolayer multiheterostructure composed with $MoS_2$-Janus MoSSe-Janus MoSeS-$MoSe_2$. (*L*) Spatially resolved Raman mapping for $A_{1g}$ mode intensity of monolayer multiheterostructures based on $MoS_2$-Janus MoSSe-Janus MoSeS-$MoSe_2$. The red area represents $MoS_2$ region, the blue area represents Janus region, and the green area represents $MoSe_2$ region.

MSSe within the same host monolayer (Fig. 3*B*). Furthermore, the chalcogen on the other side can be replaced by using a flip-over transfer (*Methods*) and another selective RT-ALS conversion, resulting in lateral multiheterostructures of $MS_2$-MSSe-MSeS-$MSe_2$ (Fig. 3*C*) with tailored functionalities. Fig. 3*D* shows the scanning electron microscopy (SEM) image of monolayer Janus MoSSe-$MoS_2$ stripe patterns with different widths. Even though both MoSSe and $MoS_2$ are semiconductors with comparable bandgaps, MoSSe is brighter than $MoS_2$, possibly due to the intrinsic vertical dipole in the monolayer. Fig. 3*E* shows the spatially resolved PL mapping of Janus MoSSe with the pattern of the Massachusetts Institute of Technology mascot "Tim the beaver" made on a continuous monolayer CVD-$MoS_2$ canvas (RT-ALS converted the exposed regions to Janus MoSSe, while the masked regions remained as pristine $MoS_2$). The same pattern was characterized using various methods: OM image (*SI Appendix*, Fig. S5*A*), SEM image (*SI Appendix*, Fig. S5*B*), and Raman and PL mappings (*SI Appendix*, Fig. S5 *C* and *D*), which all clearly verify that $MoS_2$ and MoSSe are well-located as designed. ADF-STEM is used to characterize the junction, which shows that the $MoS_2$-MoSSe interface is seamlessly connected at the boundary defined by lithography (Fig. 3*F* and *SI Appendix*, Fig. S6*A*). Elemental diffusion (2, 4) is not anticipated for the RT-ALS strategy, as the substitution occurs at room temperature within a short time. As ADF-STEM intensity scales with the atomic number, the $MoS_2$ region with weaker intensity from the S-S column on the left side of Fig. 3*F* is clearly distinguished from the stronger intensity from the S-Se column of MoSSe on the right. Additionally, the different structures of $MoS_2$ and MoSSe are further verified by the intensity profile of electron scattering, where the atomic positions of Mo, S/Se, and 2S are corresponding to their gradually decreased intensities (Fig. 3 *G* and *H*). The energy-dispersive X-ray spectroscopy results (*SI Appendix*, Fig. S6 *C–H*) indicate that Se and S atoms are well-confined in the selective regions. As the selected area electron diffraction patterns show nonseparable patterns from these two lattices (*SI Appendix*, Fig. S7 *A–D*), real space strain mappings were further performed (*SI Appendix*, Fig. S7 *G* and *H*), in which the slight lattice difference in the MoSSe region can be observed compared to the reference $MoS_2$ region.

Flipping over the $MoS_2$-MoSSe heterostructures and repeating selective RT-ALS on the other side yielded lateral multiheterostructures with $MoS_2$, Janus MoSSe and MoSeS, and $MoSe_2$ (Fig. 3 *I–L* and *SI Appendix*, Fig. S8). From the OM image in Fig. 3*I*,



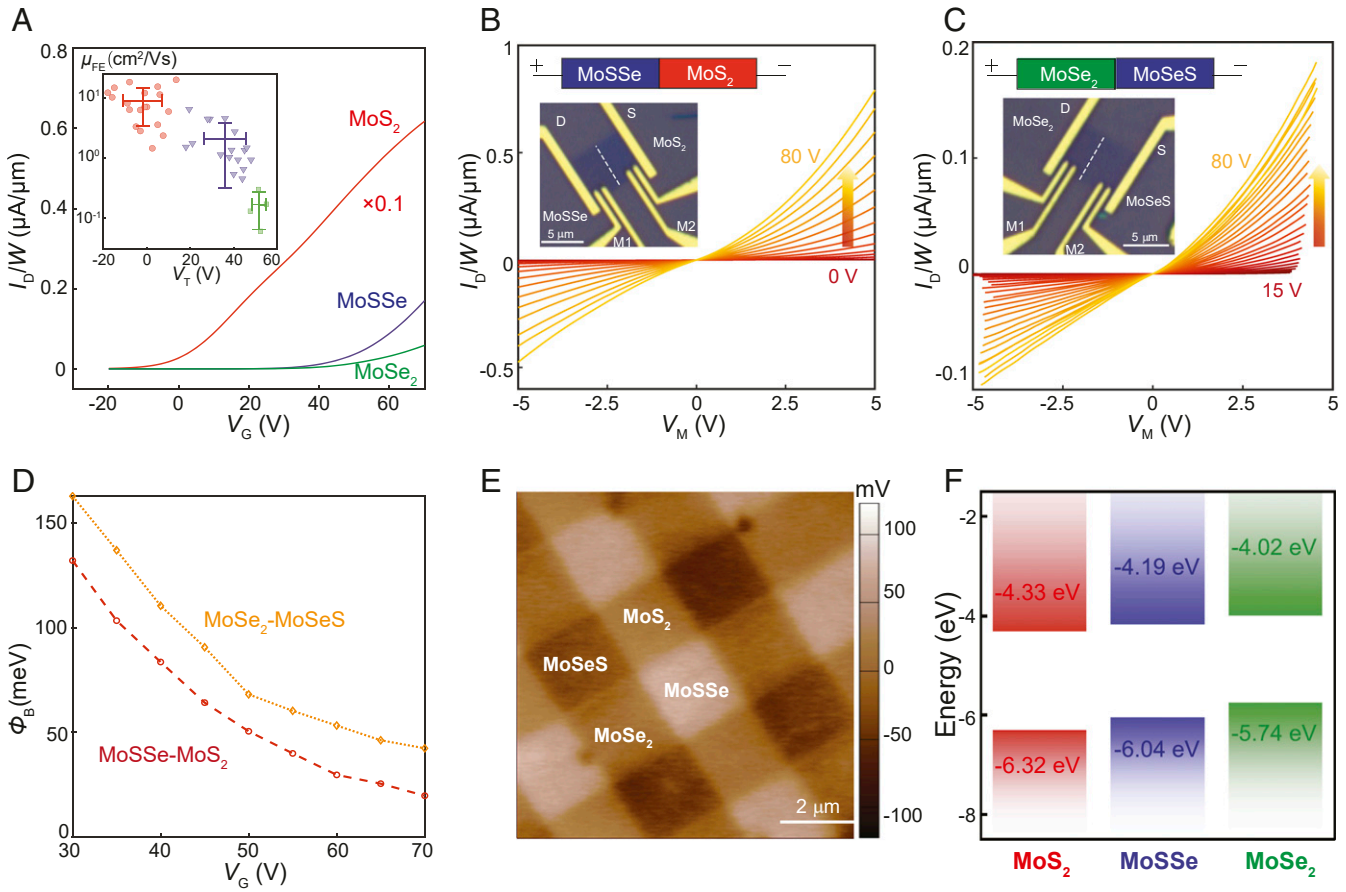


**Fig. 4.** Electrical properties of $MoS_2$, Janus MoSSe, $MoSe_2$, and their lateral heterostructures produced by ALS. (*A*) Transfer characteristics (current density $I_D/W$ versus back-gate voltage $V_G$, $V_D = 1$ V) of typical $MoS_2$, single-side-converted Janus MoSSe, and double-side-converted $MoSe_2$. (*Inset*) Field effect mobility $\mu_{FE}$ versus threshold voltage $V_T$ for tens of devices. The average mobility values for $MoS_2$, Janus MoSSe, and $MoSe_2$ are 8.94, 2.11, and 0.17 $cm^2/Vs$, and the average $V_T$ for them are −1.9, 36.0, and 51.6 V, respectively. (*B* and *C*) Four-probe output characteristics (current density $I_D/W$ versus bias voltage $V_M$ with various back-gate voltage $V_G$) for (*A*) MoSSe-$MoS_2$ and (*B*) MoSeS-$MoSe_2$ lateral heterojunctions. (*Insets*) Diagrams and OM images of these devices. (*D*) Barrier height $\Phi_B$ as a function of $V_G$ for the MoSSe-$MoS_2$ (red) and the MoSeS-$MoSe_2$ (orange) lateral heterojunctions. (*E*) Kelvin probe force microscope image of the $MoS_2$-MoSSe-MoSeS-$MoSe_2$ multiheterostructure. The Janus MoSSe region with the Se layer on top and the MoSeS region with the S layer on top display the highest and the lowest surface potential, respectively, whereas the surface potentials for the $MoS_2$ and $MoSe_2$ regions are in between. (*F*) Conduction band minima and valence band maxima energies of $MoS_2$, Janus MoSSe, and $MoSe_2$ relative to vacuum, obtained from DFT calculations. For Janus MoSSe, the vacuum energy levels from upper and lower planes are averaged.

it can be seen that Janus MoSSe and Janus MoSeS has very similar optical contrast, while the AFM image Fig. 3*J* indicates the slight height increase after each RT-ALS step, consistent with the observation from *SI Appendix*, Fig. S2 *E–G*. Fig. 3*K* shows the SEM of the multiheterostructure regions. The two types of Janus regions (MoSSe [having vertical dipole pointing up] and MoSeS [having vertical dipole point down]) demonstrates clear intriguing contrast under SEM. These two types of regions should have very similar properties (e.g., material composition, bandgap, etc.) except the dipole direction, such observation indicates the role played by the dipole moment in material functionalities. In Fig. 3*L*, spatially resolved Raman mapping for $A_{1g}$ mode intensity of such monolayer multiheterostructures is presented, with the red region being $MoS_2$, blue region being Janus (either MoSSe or MoSeS), and green region being converted $MoSe_2$.

In principle, the minimum feature size of RT-ALS should be determined by the resolution of lithography (Fig. 3*D* and *SI Appendix*, Fig. S5 *E–H*). With current EBL, features of hundreds of nanometers can be achieved, with potential for scaling down to tens of nanometers using extreme ultraviolet, helium-beam, or AFM-based lithography (28). The interface revealed by ADF-STEM (Fig. 3*F*) indicates edge roughness due to EBL limitations. However, sharp edges are anticipated if atomically sharp physical masks such as aligned carbon nanotubes (29, 30) can be used in the future. Nevertheless, even with the current EBL, many new device structures with unusual physical properties and potential applications can already be envisioned. For example, periodic arrays of these planar heterostructures with 100-nm-scale pitch can be defined as an atomically thin optical grating, and metasurfaces for efficient modulation or steering of visible/near-infrared light can be designed. In these structures, the extremely strong light-matter interactions in 2D materials and the optical nonlinearity in Janus TMD (31, 32) could play critical roles in expanding the design space of these atomically thin optical metasurfaces with unprecedented efficiencies or novel functionalities. The ability to create these artificial TMD multiheterostructures within a continuous atomic-layer "canvas" has never been achieved before and presents extremely exciting potentials.

A major application of 2D materials and their heterostructures lies in novel electronic or optoelectronic devices. With RT-ALS, we found that high-quality materials are obtained, and the energy misalignment of band edges exist at both the MoSSe-$MoS_2$ and $MoSe_2$-MoSeS lateral heterojunctions with a type-II band alignment. Multiple back-gate transistors with long and short electrodes were fabricated and four-probe measurements were used to eliminate the contact resistance (OM images in Fig. 4 *B* and *C*, Insets). Typical transfer characteristics (channel current $I_D$ versus back-gate voltage $V_G$) are plotted in Fig. 4*A* and used to extract the threshold voltage $V_T$, defined as the intersection of the linear fit of the on-current and the x-axis, and the field effect mobility $\mu_{FE}$, defined as $\mu_{FE} = (L/W)g_m/(V_D C_{ox})$, where $L$ and $W$ are the channel length and channel width, $g_m$ is the transconductance, $V_D$ is the source-drain voltage (bias across the channel), and $C_{ox} = 12.1$ nF/cm$^2$ (capacitance of the 285 nm $SiO_2$ gate oxide). The $V_T$ and $\mu_{FE}$ of tens of devices were measured for the starting CVD $MoS_2$, single-side-converted Janus MoSSe, as well as double-side-converted $MoSe_2$, summarized in Fig. 4*A*, Inset. Average $\mu_{FE}$ for $MoS_2$, Janus MoSSe, and ALS $MoSe_2$ are 8.94 cm$^2$/Vs, 2.11 cm$^2$/Vs, and 0.17 cm$^2$/Vs, respectively. Average $V_T$ for them are −1.9 V, 36.0 V, and 51.6 V, respectively. The gradual degradation of mobility from $MoS_2$ to $MoSe_2$ may arise from the introduction of defects through the RT-ALS or transfer processes. Note that the mobility value measured in our Janus MoSSe devices is two orders of magnitude higher than through the route of conventional high-temperature substitution (15), which is indicative of the high quality of materials from RT-ALS. Furthermore, the increasing of $V_T$ values indicates that $MoS_2$ is the most $n$-type doped, whereas Janus MoSSe and $MoSe_2$ are decreasingly $n$-doped, in agreement with DFT calculated band alignment (Fig. 4*F*). This band alignment configuration further determines the electrical polarity of Janus MoSSe-$MoS_2$ and $MoSe_2$-Janus MoSeS lateral heterojunctions. The Janus MoSSe and the converted $MoSe_2$ regions are the anodes of these two n-n$^+$ junctions, respectively, and confirmed with output characteristics ($I_D$ versus $V_M$ with different $V_G$, where $V_M$ is the voltage drop across the two inner short electrodes [M1 and M2] as $I_D$ is applied across the two long electrodes [D and S]), as shown in Fig. 4 *B* and *C*. The weak rectification behaviors observed on both lateral junctions suggest that the barrier heights (denoted as $\Phi_B$) at the lateral heterojunctions are very low. We performed temperature-dependent four-probe transport measurement and used the thermionic emission model to extract the gate-dependent barrier heights (see *Methods* for details, and *SI Appendix*, Figs. S9 and S10), plotted in Fig. 4*D*, for $\Phi_B = 30$ meV and 50 meV for MoSSe-$MoS_2$ and $MoSe_2$-MoSeS lateral heterojunctions, respectively, when the channels are turned on completely ($V_G > 50$ V).

More uniquely, our RT-ALS approach brings about a programmable control of the out-of-plane electrical dipole in TMD materials (induced by the electronegativity difference between S and Se atoms in Janus MoSSe). We performed Kelvin probe force microscope measurements on the $MoS_2$-MoSSe-MoSeS-$MoSe_2$ grid samples (Fig. 4*E*) to observe clear surface potential differences among these four distinct materials. As expected, the Janus MoSSe region with the Se layers on top and the flipped MoSeS region with the S layers on top display the highest and the lowest surface potentials, respectively, whereas the surface potentials for the $MoS_2$ and $MoSe_2$ regions are in between. The measured potential difference between the top Se layer of the MoSSe region and the top S layer of the MoSeS region is around 100 meV. Such potential difference is even larger than that between the $MoSe_2$ and $MoS_2$ regions (which is around 15 meV), suggesting that the Janus MoSSe (or MoSeS) holds a large intrinsic dipole that is locked to the 2D surface normal. Note that this dipole can be selectively patterned to be zero ($MoS_2$, $MoSe_2$), positive (MoSSe), and negative (MoSeS) on such a 2D material "canvas," which would enable many nanostructures and devices with intriguing electrical and optoelectronic properties. For example, with proper choice of physical masks, such as e-beam resist, or carbon nanotubes (28, 29) with atomically sharp edges, it is possible to make in-plane quantum wells, superlattices, or photonic devices by generating periodic arrays of such dipole/nondipole lateral heterostructures with 1- to 100-nm periodicity. Not only can the transport and optical properties of these MoXY multiheterostrutures be altered, any materials in close vicinity would also be modulated by such an electrostatic "canvas." Unusual physical properties and unprecedented functionality may be possible on such a platform, ranging from nonlinear optics, electronic band engineering, and nanoscale origami to electrochemical catalysis, all of which can be modulated by different electrostatic forces.

In summary, the RT-ALS combined with patterning and flip transfer present a powerful yet universal strategy to program material properties at the atomic-layer limit. It allows for creating diverse artificial low-symmetry 2D materials and their heterostructures. Such a process generates seamless, high-quality interfaces between different structures and can complement existing vdW heterostructure fabrication techniques by adding another intriguing class of materials (Janus and lateral Janus heterostructures and multiheterostructures). Furthermore, by designing these heterostructure patterns and surface charge distributions, great potential is anticipated in new physical discoveries and future applications.

## Methods

**Synthesis of $MoS_2$.** A target $SiO_2$ substrate was suspended between two other $SiO_2$/Si substrates with predeposited perylene-3, 4, 9, 10-tetracarboxylic acid tetrapotassium solution. All of these substrates were placed facedown on a crucible containing $MoO_3$ precursor in a 1-inch quartz tube. This crucible was placed in the middle of the heating zone with another sulfur crucible on the upstream. Before heating, the whole CVD system was purged with 1,000 sccm Ar (99.999% purity) for 3 min. Then, 20 sccm Ar was introduced into the system as a carrier gas. The growth system was heated to 625 °C for 15 min. The $MoS_2$ growth was carried out around 620 to 630 °C for 3 min under atmospheric pressure. After growth, the whole system was naturally cooled down to room temperature.

**Plasma-Assisted ALS.** We use a remote commercial inductively coupled plasma system to substitute the top-layer sulfur atoms of monolayer $MS_2$ (M = Mo, W) with selenium. The CVD grown monolayer $MoS_2$/$WS_2$ were placed in the middle of a quartz tube. The plasma coil made by a cylindrical copper tube placed at the upstream of CVD furnace. The distance between the sample and the plasma coil is around 8 to 10 cm, with the selenium powder placed around 5 cm away from the plasma generator on the other side. Whenever masks were needed, the sample was covered with PMMA patterns defined by EBL. At the beginning of the process, the whole system was pumped down to a low pressure to remove air in the chamber. Then, hydrogen was introduced into the system and the plasma generator was ignited. The hydrogen atoms assist the removal of the sulfur atoms on the top layer of $MoS_2$. At the same time, the vaporized selenium filled in the vacancy of the sulfur atoms, resulting in the asymmetric Janus structure of MoSSe. The whole process was performed at room temperature. After the reaction, the whole system was purged with Ar gas (99.999% purity) to remove the residual reaction gas, and the pressure was recovered to atmospheric.

**Transfer.** For normal transfer, the samples were spin-coated with PMMA as a supporting layer. Then, they were put in the KOH solution and the PMMA/2D material was detached from the growth substrate and was floated on the surface of KOH solution. Afterward, it was taken to a deionized (DI) water bath by a glass slide and washed several times and then picked up with the target substrate. After baking on a hot plate at 100 °C for 15 min, the PMMA layer was removed with acetone and isopropanol (IPA). For flip-over transfer, the premade MoSSe sample was picked up by a polydimethylsiloxane stamp and then was released onto an intermediate substrate. Then, the MoSSe was released through etching the $SiO_2$ in a KOH solution. The film was washed with DI water for several times and then put upside-down on the target $SiO_2$/Si substrate, with the bottom-layer selenium atoms touching the substrate. At last, the PMMA film was removed by acetone and IPA.

**Data Availability.** All study data are included in the article and/or *SI Appendix*. All materials are available upon request to J.K.

**ACKNOWLEDGMENTS.** The preliminary experiments of this work are supported by the Air Force Office of Scientific Research under the Multidisciplinary University Research Initiative (MURI)-FATE program, Grant No. FA9550-15-1-0514. The characterization of the Janus Materials at a later stage was supported by the US Department of Energy (DOE), Office of Science, Basic Energy Sciences under Award DE-SC0020042. Y.L. and T.P. acknowledge the US Army Research Office through the Institute for Soldier Nanotechnologies under Cooperative Agreement No. W911NF-18-2-0048 and the Science-Technology Center (STC) for Integrated Quantum Materials, NSF Grant No. DMR 1231319. P.-C.S. and A.-Y.L. acknowledge the funding from the Center for Energy Efficient Electronics Science (NSF Award No. 0939514) and the US Army Research Office through the Institute for Soldier Nanotechnologies at Massachusetts Institute of Technology, under Cooperative Agreement No. W911NF-18-2-0048. K.X. and T.C. are partially supported by NSF through the University of Washington Materials Research Science and Engineering Center Grant No. DMR-1719797. K.X. acknowledges support by the state of Washington through the University of Washington Clean Energy Institute. B.Y. and Y.Y. acknowledge the funding from Natural Science Foundation of China (Grant No. 21805184), NSF Shanghai (Grant No. 18ZR1425200), and the Center for High-resolution Electron Microscopy at ShanghaiTech University (Grant No. EM02161943). C.S. and J.W. acknowledge support through US Army Research Office under Grant No. W911NF-18-1-0431. Q.J. acknowledges support from the STC Center for Integrated Quantum Materials, NSF Grant No. DMR 1231319. S.H. and K.Z. acknowledge financial support from NSF (ECCS-1943895). L.D. acknowledges support from the US Department of Defense, Office of Naval Research (Grant No. N00014-19-1-2296). E.S. acknowledges support from the Davidson School of Chemical Engineering of Purdue University. J.L. and C.S. acknowledge support from an Office of Naval Research MURI (Grant No. N00014-17-1-2661). The crystallographic tilted STEM image research was conducted at the Center for Nanophase Materials Sciences, which is a DOE Office of Science User Facility (J.-C.I.). We thank X. Zhang, Y. Han, G. Cheng, N. Yao, and N. Yan for helpful discussions.

1. Y. Gong *et al*., Vertical and in-plane heterostructures from $WS_2$/$MoS_2$ monolayers. *Nat. Mater.* **13**, 1135–1142 (2014).
2. C. Huang *et al*., Lateral heterojunctions within monolayer $MoSe_2$-$WSe_2$ semiconductors. *Nat. Mater.* **13**, 1096–1101 (2014).
3. M. Y. Li *et al*., NANOELECTRONICS. Epitaxial growth of a monolayer WSe2-MoS2 lateral p-n junction with an atomically sharp interface. *Science* **349**, 524–528 (2015).
4. P. K. Sahoo, S. Memaran, Y. Xin, L. Balicas, H. R. Gutiérrez, One-pot growth of two-dimensional lateral heterostructures via sequential edge-epitaxy. *Nature* **553**, 63–67 (2018).
5. R. Xiang *et al*., One-dimensional van der Waals heterostructures. *Science* **367**, 537–542 (2020).
6. Z. Zhang *et al*., Robust epitaxial growth of two-dimensional heterostructures, multiheterostructures, and superlattices. *Science* **357**, 788–792 (2017).
7. S. Xie *et al*., Coherent, atomically thin transition-metal dichalcogenide superlattices with engineered strain. *Science* **359**, 1131–1136 (2018).
8. C. Wang *et al*., Monolayer atomic crystal molecular superlattices. *Nature* **555**, 231–236 (2018).
9. Y. Cao *et al*., Unconventional superconductivity in magic-angle graphene superlattices. *Nature* **556**, 43–50 (2018).
10. Y. Cao *et al*., Correlated insulator behaviour at half-filling in magic-angle graphene superlattices. *Nature* **556**, 80–84 (2018).
11. R. Ribeiro-Palau *et al*., Twistable electronics with dynamically rotatable heterostructures. *Science* **361**, 690–693 (2018).
12. A. Y. Lu *et al*., Janus monolayers of transition metal dichalcogenides. *Nat. Nanotechnol.* **12**, 744–749 (2017).
13. J. Berry, S. Ristić, S. Zhou, J. Park, D. J. Srolovitz, The MoSeS dynamic omnigami paradigm for smart shape and composition programmable 2D materials. *Nat. Commun.* **10**, 5210 (2019).
14. D. B. Trivedi *et al*., Room-temperature synthesis of 2D Janus crystals and their heterostructures. *Adv. Mater.* **32**, e2006320 (2020).
15. J. Zhang *et al*., Janus monolayer transition-metal dichalcogenides. *ACS Nano.* **11**, 8192–8198 (2017).
16. Y.-C. Lin *et al*., Low energy implantation into transition-metal dichalcogenide monolayers to form Janus structures. *ACS Nano.* **14**, 3896–3906 (2020).
17. H.-P. Komsa *et al*., Two-dimensional transition metal dichalcogenides under electron irradiation: Defect production and doping. *Phys. Rev. Lett.* **109**, 035503 (2012).
18. M. Ghorbani-Asl, S. Kretschmer, D. E. Spearot, A. V. Krasheninnikov, Two-dimensional MoS2 under ion irradiation: From controlled defect production to electronic structure engineering. *2D Mater.* **4**, 025078 (2017).
19. Z. Li *et al*., Low-temperature growth of graphene by chemical vapor deposition using solid and liquid carbon sources. *ACS Nano.* **5**, 3385–3390 (2011).
20. W. H. Chiang, R. M. Sankaran, Synergistic effects in bimetallic nanoparticles for low temperature carbon nanotube growth. *Adv. Mater.* **20**, 4857–4861 (2008).
21. S. J. Yun *et al*., Telluriding monolayer $MoS_2$ and $WS_2$ via alkali metal scooter. *Nat. Commun.* **8**, 2163 (2017).
22. J. A. Phillips, Charge equilibrium ratios for hydrogen ions from solids. *Phys. Rev.* **97**, 404 (1955).
23. S.-H. Su *et al*., Controllable synthesis of band-gap-tunable and monolayer transition-metal dichalcogenide alloys. *Front. Energy Res.* **2**, 27 (2014).
24. M. Mahjouri-Samani *et al*., Patterned arrays of lateral heterojunctions within monolayer two-dimensional semiconductors. *Nat. Commun.* **6**, 7749 (2015).
25. X. Wang *et al*., Chemical vapor deposition growth of crystalline monolayer $MoSe_2$. *ACS Nano.* **8**, 5125–5131 (2014).
26. C. X. Xia *et al*., Universality of electronic characteristics and photocatalyst applications in the two-dimensional Janus transition metal dichalcogenides. *Phys. Rev. B* **98**, 165424 (2018).
27. L. Liu *et al*., Phase-selective synthesis of 1T′ $MoS_2$ monolayers and heterophase bilayers. *Nat. Mater.* **17**, 1108–1114 (2018).
28. A. Balčytis *et al*., "High precision fabrication of antennas and sensors" in *Proceedings of the Ninth International Symposium on Precision Engineering Measurement and Instrumentation* **Vol. 9446**, J. Cui, J. Tan, X. Wen, Eds. (International Society for Optics and Photonics, Changsha/Zhangjiajie, China, 2014), 94461G-1 to 94461G-11.
29. L. Liu *et al*., Aligned, high-density semiconducting carbon nanotube arrays for high-performance electronics. *Science* **368**, 850–856 (2020).
30. X. He *et al*., Wafer-scale monodomain films of spontaneously aligned single-walled carbon nanotubes. *Nat. Nanotechnol.* **11**, 633–638 (2016).
31. A. C. Riis-Jensen, T. Deilmann, T. Olsen, K. S. Thygesen, Classifying the electronic and optical properties of Janus monolayers. *ACS Nano* **13**, 13354–13364 (2019).
32. M. Palsgaard, T. Gunst, T. Markussen, K. S. Thygesen, M. Brandbyge, Stacked Janus device concepts: Abrupt pn-junctions and cross-plane channels. *Nano Lett.* **18**, 7275–7281 (2018).

# Supplementary Information for

## Designing Artificial Two-Dimensional Landscapes *via* Atomic-Layer Substitution

Yunfan Guo[1‡]*, Yuxuan Lin[1‡], Kaichen Xie[2‡], Biao Yuan[3], Jiadi Zhu[1], Pin-Chun Shen[1], Ang-Yu Lu[1], Cong Su[4], Enzheng Shi[5,10], Kunyan Zhang[6], Changan HuangFu[7], Haowei Xu[4], Zhengyang Cai[1], Ji-Hoon Park[1], Qingqing Ji[1], Jiangtao Wang[1], Xiaochuan Dai[1], Xuezeng Tian[8], Shengxi Huang[6], Letian Dou[5], Liying Jiao[7], Ju Li[4], Yi Yu[3], Juan-Carlos Idrobo[9], Ting Cao[2], Tomás Palacios[1], Jing Kong[1]*

[1]Department of Electrical Engineering and Computer Science, Massachusetts Institute of Technology, Cambridge MA 02139, United States

[2]Department of Materials Science & Engineering, University of Washington, Seattle, WA, 98195, United States

[3]School of Physical Science and Technology, ShanghaiTech University, Shanghai 201210, China.

[4]Department of Nuclear and Materials Science and Engineering, Massachusetts Institute of Technology, Cambridge MA 02139, United States

[5]Davidson School of Chemical Engineering, Purdue University, West Lafayette, Indiana 47907, United States.

[6]Department of Electrical Engineering, The Pennsylvania State University, University Park, Pennsylvania 16802, United States

[7]Key Laboratory of Organic Optoelectronics and Molecular Engineering of the Ministry of Education, Department of Chemistry, Tsinghua University, Beijing 100084, China.

[8]Beijing National Laboratory for Condensed Matter Physics, Institute of Physics, Chinese Academy of Sciences, Beijing 100190, China

[9]Center for Nanophase Materials Sciences, Oak Ridge National Laboratory, Oak Ridge, TN, 37831, United States

[10]Key Laboratory of 3D Micro/Nano Fabrication and Characterization of Zhejiang Province, School of Engineering, Westlake University, 18 Shilongshan Road, Hangzhou 310024, China.

*To whom correspondence should be addressed: jingkong@mit.edu (J.K.); yfguo112@mit.edu. (Y.G.).

‡These authors contributed equally to this work.

## Supplementary Text

**Raman and photoluminescence spectroscopy:** Raman and PL spectra were performed on a Horiba Jobin-Yvon HR800-confocal Raman Spectrometer. The laser excitation wavelength for Raman and PL measurements was 532.5 nm. A 100X objective was used to focus the laser beam. The laser power on the sample was about 0.1 mW. For PL and Raman mapping, the scanning step size is ~0.5 μm.

**Transmission electron microscopy:** The atomic structure of $MoS_2$-MoSSe lateral heterostructure was acquired using JEOL TEMs. The ADF-STEM image was taken on a 300 kV aberration-corrected JEOL GrandARM. The diffraction patterns were obtained on a 200 kV JEOL JEM-2100plus. The EDS mapping was collected on a 120 kV JEOL JEM-1400. The ADF-STEM experimental conditions were: condenser lens aperture 20 μm, probe size 9c, the probe current 7.3 pA, and camera length 15 cm, which corresponds to an inner collection angle of 42 mrad and outer collection angle of 180 mrad. The strain mapping is measured based on the geometric phase analysis using MacTempasX (1) software. The crystallographic tilted STEM images were obtained in an aberration-corrected Nion UltraSTEM 100$^{TM}$ operated at 100 kV, using a convergence semiangle of 30 mrad.

**KPFM:** KPFM measurements were performed using a Cypher AFM system (Asylum Research) with Ti/Ir-coated cantilevers (ASYELEC-01, Oxford Instruments) with a nominal mechanical resonant frequency and spring constant of 70 kHz and 2 N/m, respectively. The two-pass scanning method consists of a surface topography scanning and a nap mode which lifts up the tip and keep at a constant distance at 30 nm while scanning. During the nap mode, an AC bias is applied to the tip for tip vibration, and a DC voltage is applied between the tip and sample to minimize the vibration amplitude. The signal of DC voltage can be used qualitatively as a reflection of surface potential change, but there are still other factors may influence the tip vibration.

**Fabrication and transport measurements:** The as-grown MoSSe-$MoS_2$ or $MoSe_2$-MoSeS heterostructures were first transferred onto a 285 nm $SiO_2$/Si substrate. An EBL step and an electron-beam evaporation step (30 nm Ni/30 nm Au) were used to define the metal contacts. Another EBL step and a reactive ion etching process ($O_2$ plasma) were performed to etch the 2D material and define the channel regions. The transport measurements were carried out using a

semiconductor parameter analyzer (Agilent 4155C) in a cryogenic probe station (Lakeshore) with a temperature controller and liquid nitrogen cooling. The pressure of the chamber was kept below $5\times10^{-6}$ torr.

To extract the barrier height at the lateral heterojunctions, a reverse-bias thermionic emission model is used (2):

$$\ln\left(\frac{|I_R|}{T^{3/2}}\right) = \ln(A^*) - \frac{q\Phi_B}{k_B T}$$

Here $I_R$ is the reverse bias (-0.1 V) current, $T$ is the temperature, $A^*$ is the effective Richardson's constant, $k_B$ is the Boltzmann constant, $q$ is the electron charge, and $\Phi_B$ is the barrier height. The output characteristics of the MoSSe-$MoS_2$ and the $MoSe_2$-MoSeS lateral heterojunctions are plotted in Extended Data Fig. 9. The Arrhenius plot ($\ln(|I_R|/T^{3/2})$ versus $1000/T$) is plotted in Extended Data Fig. 10. For the 4-probe measurements, a drain-to-source voltage $V_D$ was applied to the device, and the drain current $I_D$ and the voltage drop $V_M$ across the two short electrodes (M1 and M2) was measured. Because there are no current following into M1 and M2, there is no voltage drop on the M1-channel and M2-channel contact ($V$=$IR$). As a result, the measured $V_M$ is completely from the channel part (from M1 to M2). In this way, the influence of the contact resistance can be eliminated if we plot $I_D$ versus $V_M$.

**Theoretical Calculations:** Ab initio calculations were performed using density functional theory in the Perdew–Burke–Ernzerhof exchange-correlation functional with dispersion correction (PBE-D2), implemented in the Quantum Espresso package (3). A supercell arrangement was used with the cell dimension in the out-of-plane direction set at 20 Å to avoid interactions between the transition metal dichalcogenide layers and its periodic images. Both 2×2 and 3×3 supercells have been used. We use ultrasoft pseudopotentials with a plane-wave energy cutoff of 40 Ry. The structures were fully relaxed until the force on each atom is <0.005 eV/Å. Spin-orbit coupling was not included in our reaction path calculations.

The band alignments were obtained using DFT method in the Heyd–Scuseria–Ernzerhof (HSE06) hybrid functional (4) with dispersion correction, with structures relaxed by DFT method in the PBE functional with dispersion correction. We use norm-conserving pseudopotentials with a plane-wave energy cutoff of 100 Ry. Spin-orbit coupling was included in the band alignment

calculations. We note that the Kohn–Sham band gaps from DFT do not explicitly include the quasiparticle self-energy corrections. However, the self-energies corrections to the band gaps in $MoS_2$ and $MoSe_2$ have been shown to be very similar (5). As a result, the conduction (or valence) band alignment should be relatively insensitive to the self-energy corrections.

For the prediction of Raman peaks of monolayer 1T' Janus MoSSe, DFT calculations were performed with the Vienna ab initio simulation package (VASP). We first obtained the phonon frequencies $f$ and displacement modes $Q$ with density functional perturbation theory. Then the Raman tensor $P$ were calculated with $P \propto \frac{\mathrm{d}\epsilon}{\mathrm{d}Q}$, which is the derivative of the macroscopic dielectric tensor $\epsilon$ with respect to the phonon displacement modes $Q$. The Raman activities of 1T' MoSSe are shown in Figure S3k.

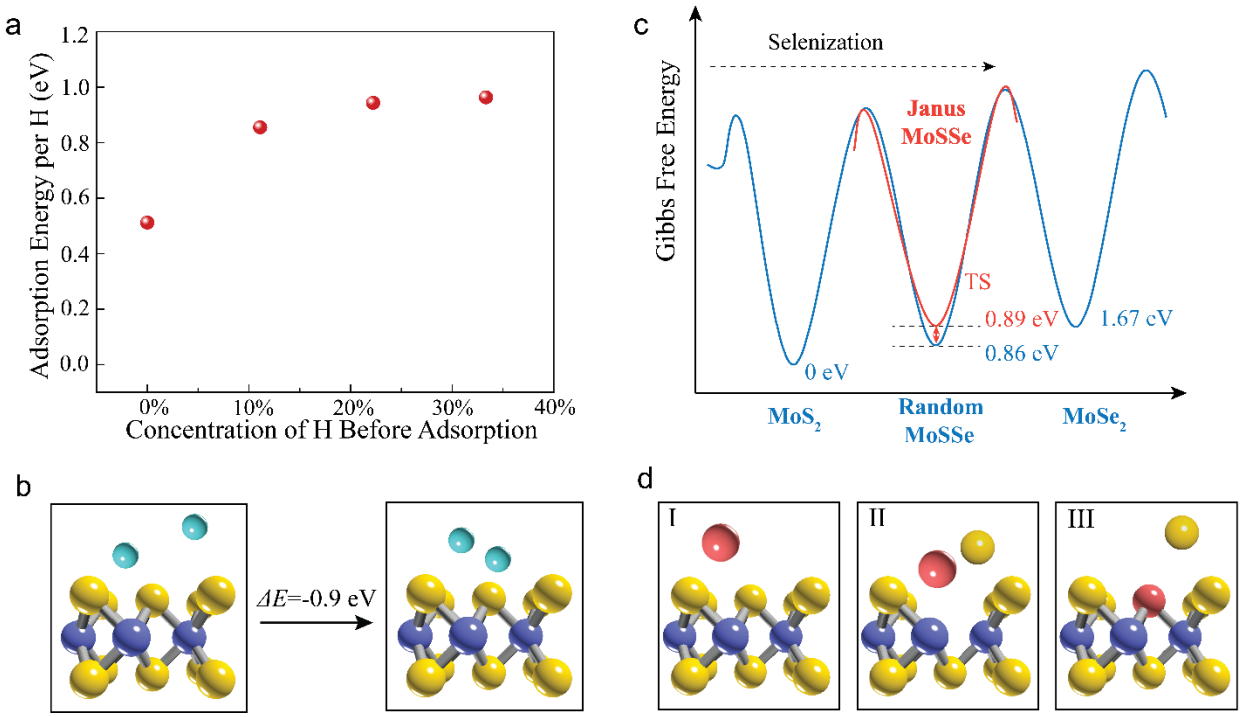


**Figure S1. a,** Adsorption energy of H as a function of H concentration before adsorption for $MoS_2$ and Janus MoSSe. The adsorption energy (per H) on the $MoS_2$ and Janus MoSSe monolayer shows an increasing trend with the hydrogen coverage. We calculate the adsorption energies of hydrogen atoms in a 3x3 supercell at different coverage percentages. At the dilute limit, the adsorption is largest if H sits on the S atom. For calculations with multiple H atoms in the supercell, the H are initially placed at positions such that the distance between pairs of H are maximized. The increment of adsorption energy with the coverage rate makes the high H density on the $MoS_2$ surface possible, which later facilities the S desorption. At coverage rate of H after adsorption> 50%, $H_2$ molecules would form. **b,** The hydrogen atoms diffuse on the TMD surface. As the two individual H adsorbents diffuse onto the same S atom, the total energy of the system decreases by 0.9 eV. Purple, yellow, and green balls are Mo, S, and H atoms, respectively. **c,** Free energy of $MoS_2$ (including two Se atoms in the gas phase), MoSSe (including one S and one Se atom in the gas phase), and $MoSe_2$ (including two S atoms in the gas phase) per unit cell. Their free energies are defined as $G_{MoS_2} = E_{MoS_2} + 2\mu_{Se(g)}$ , $G_{MoSe_2} = E_{MoS_{e2}} + 2\mu_{S(g)}$ , $G_{Janus\ MoSSe} = E_{Janus\ MoSSe} + \mu_{Se(g)} + \mu_{S(g)}$, and , $G_{Random\ MoSSe} = E_{Janus\ MoSSe} + \mu_{Se(g)} + \mu_{S(g)} - TS$. (Here, T is temperature, S is entropy, $\mu$ is the chemical potential of reactant.) The entropy term here refers to the configurational entropy ($S = k_B \ln \Omega$) which contributes to the free energy by $-2 \times T \times k_B \times \ln 2 = -0.03\ eV$ (the first factor 2 comes from 2 chalcogenide atoms per unit cell). If $G_{MoS_2}$ is set as a reference point equal to 0 eV, $G_{MoSe_2} = 1.67$ eV, $G_{Janus\ MoSSe} = 0.89$ eV, $G_{Random\ MoSSe} = 0.86$ eV. **d,** Reaction path in high-temperature substitution: Se adsorption on surface (I), Mo-S bond breaking and Mo-Se bond forming (S vacancy formation, II), and Se occupation of S site (III). Purple, yellow and red balls are Mo, S and Se atoms, respectively.

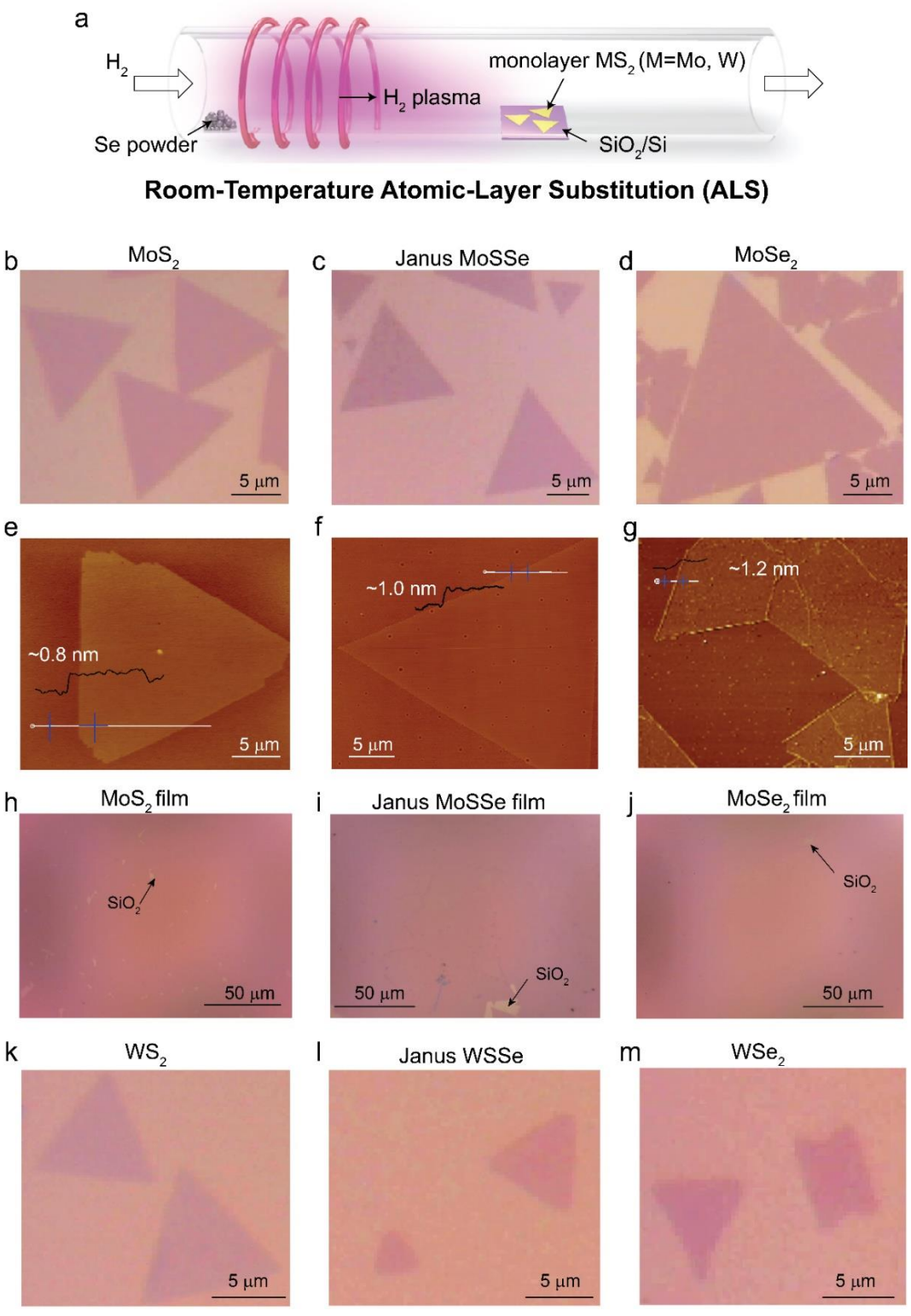


**Figure S2. Morphology characterizations for room-temperature atomic-layer substitution (RT-ALS) from monolayer $MoS_2$ to Janus MoSSe and to $MoSe_2$. a,** Schematic illustration of a remote plasma-assisted CVD system for the RT-ALS from monolayer $MS_2$. **b-d,** OM images of monolayer $MoS_2$, Janus MoSSe and converted $MoSe_2$ flakes on $SiO_2$/Si substrates, respectively.

The Janus MoSSe and converted $MoSe_2$ flakes remain intact over the conversion process. **e-g,** AFM images and the corresponding height profiles of monolayer $MoS_2$, Janus MoSSe and $MoSe_2$ flakes, respectively. It appears there is a slight height increase after each RT-ALS step, possibly due to the fact S atoms are replaced by Se atoms. **h-j,** Lower magnification OM images of continuous monolayer $MoS_2$, Janus MoSSe, and converted $MoSe_2$ films, respectively. The images were taken at locations with some exposed substrates in order to optically distinguish the film. **k-m,** OM images of monolayer $WS_2$, Janus WSSe, and converted $WSe_2$ flakes on $SiO_2$/Si substrates, respectively.

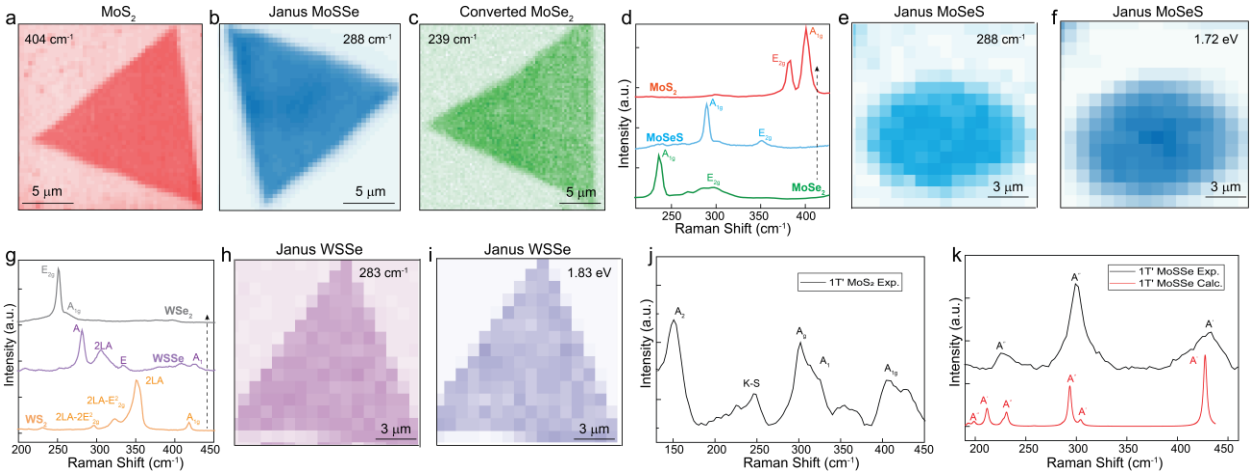


**Figure S3. Spectroscopy and morphology characterizations for RT-ALS conversion from monolayer $MX_2$ (M=Mo, W) to Janus MXY and to converted $MY_2$ (X, Y correspond to either S or Se).** **a-c,** The corresponding $A_{1g}$ Raman mappings of monolayer $MoS_2$, Janus MoSSe, and converted $MoSe_2$ in Fig. 2(a). **d,** Raman spectra of monolayer $MoSe_2$, Janus MoSeS, and converted $MoS_2$. **e** and **f,** Spatial resolved Raman and PL mappings for monolayer Janus MoSeS. **g,** Raman spectra of monolayer $WS_2$, Janus WSSe, and converted $WSe_2$. **h** and **i,** Spatially resolved Raman and PL mappings for monolayer Janus WSSe. **j,** Experimental Raman spectra of monolayer 1T' $MoS_2$. **k,** Theoretical and experimental Raman spectra of monolayer 1T' Janus MoSSe.

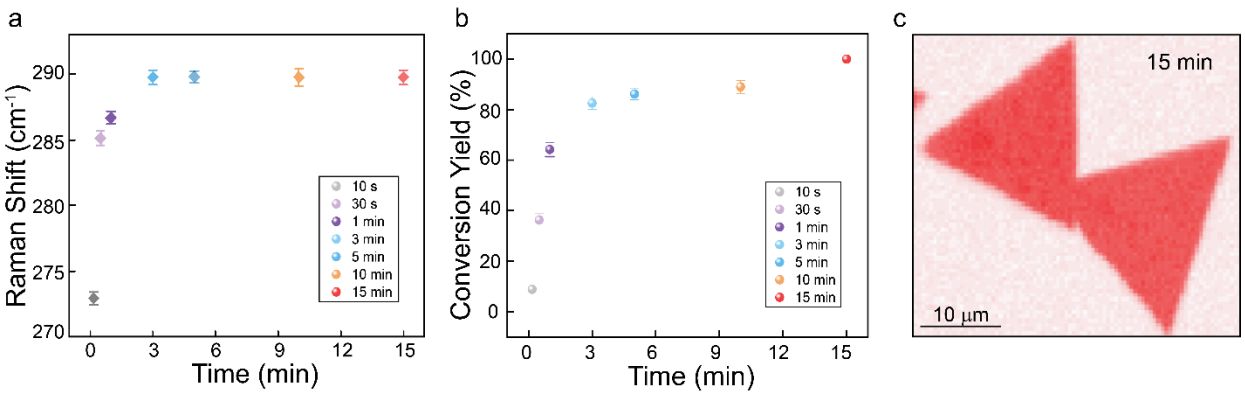


**Figure S4. Time evolution of the RT-ALS process (from monolayer $MoS_2$ to Janus MoSSe) via Raman spectra characterization. a,** The relationship between the conversion time and the Raman shift of $A_{1g}$ mode for Janus MoSSe. **b,** The relationship between the conversion time and conversion yield of Janus MoSSe. **c,** Spatially-resolved Raman mapping of two coalesced Janus MoSSe flakes converted within 15 min, which shows uniform Raman intensity over the whole MoSSe regions.

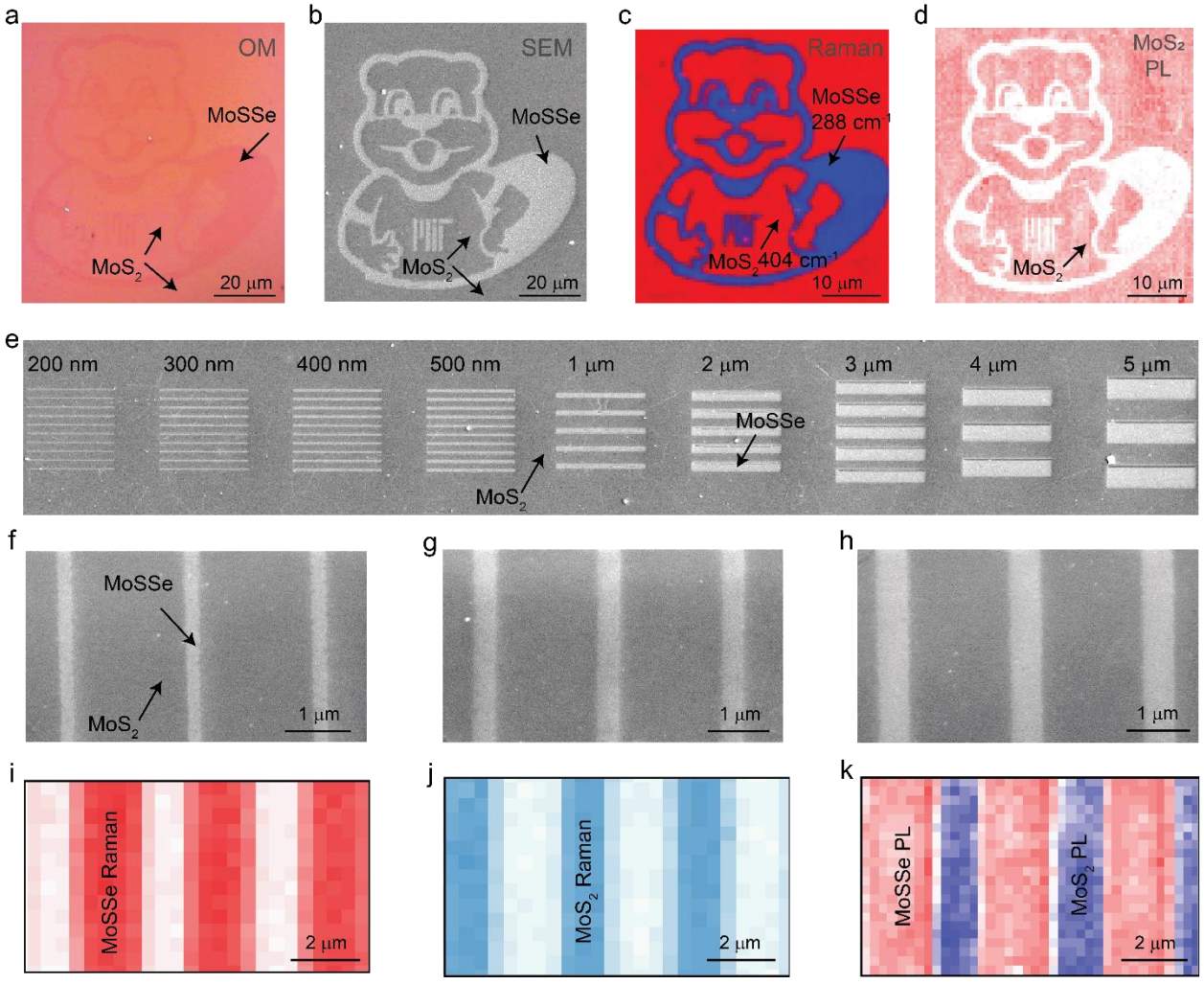


**Figure S5. Morphology and spectroscopy characterizations for the monolayer $MoS_2$-Janus MoSSe lateral heterostructure. a,** OM image of a MIT mascot "Tim the beaver" pattern (Janus MoSSe) on a $MoS_2$ canvas. **b,** SEM image of a MIT mascot "Tim the beaver" pattern (Janus MoSSe) on a $MoS_2$ canvas. **c,** Spatially- resolved Raman mapping of lateral heterostructure between $MoS_2$ and MoSSe. **d,** Spatially- resolved PL mapping of $MoS_2$. **e,** The SEM image of monolayer Janus MoSSe-$MoS_2$ stripe patterns with different widths. **f-h,** The corresponding enlarged magnification SEM images of Janus MoSSe-$MoS_2$ stripe patterns as shown in **(e). i-j,** Spatially-resolved Raman mappings of $A_{1g}$ mode for MoSSe and $MoS_2$, respectively. **k,** The PL mapping of the Janus MoSSe-$MoS_2$ lateral heterostructure.

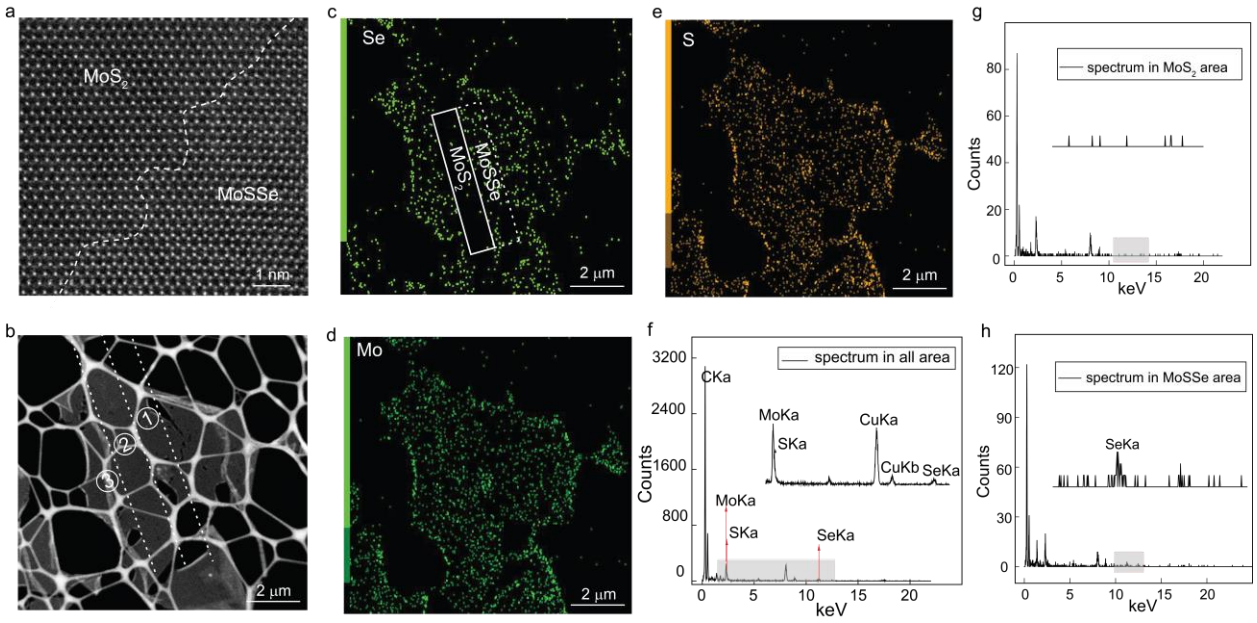


**Figure S6. TEM characterizations for $MoS_2$-MoSSe lateralheterostructures. a,** ADF-STEM image of $MoS_2$-MoSSe heterostructure. **b,** Low-magnification TEM image of $MoS_2$-MoSSe heterostructure. **c-e,** EDS mappings of $MoS_2$-MoSSe heterostructure, including the elemental mapping of Se **(c)**, Mo **(d)** and S **(e)**, respectively. **f,** EDS Spectrum in the whole area identifying the specimen as Mo, S, Se, corresponding to 2.293 eV (Mo La), 2.307 eV (S Ka) and 11.207 (Se Ka). The grey region in the main panel is enlarged and plotted as an inset in the middle. **g,** Extracted EDS spectrum of $MoS_2$ region in **(c)**. The grey region in the main panel is enlarged and plotted as an inset in the middle, showing that there is almost no Se signal in the $MoS_2$ region. **h,** Extracted EDS spectrum of MoSSe region in **(c)**. The grey region in the main panel is enlarged and plotted as an inset in the middle, showing that there is Se signal in the MoSSe region.

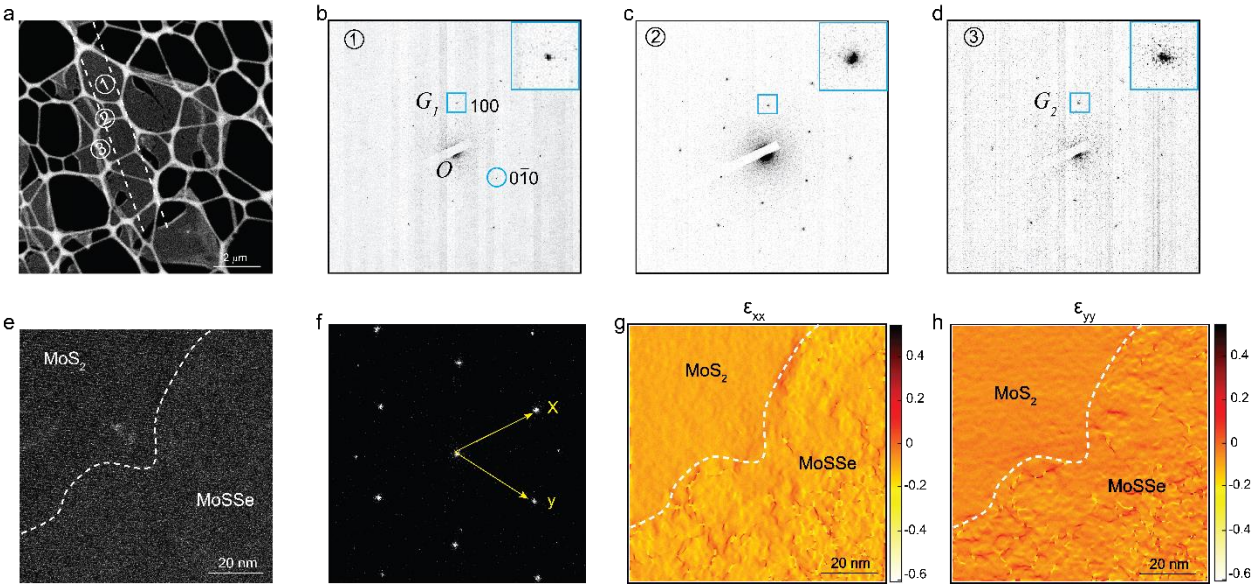


**Figure S7. a,** Low-magnification TEM image of $MoS_2$-MoSSe lateral heterostructure. **b-d,** SAED patterns of $MoS_2$ area **(b)**, the interface of $MoS_2$-Janus MoSSe heterostructure **(c)**, and the MoSSe area **(d)**, respectively. These inset images represent the individual enlarged diffraction spots. The O and G represent transmitted electron beam and diffracted electron beam, respectively. The enlarged diffracted spot in **(c)** demonstrates a dispersive but un-split spot. It implies the lattice misfit is quite small. The experimental lattice misfit calculated from experimental SAED pattern **(b and d)** is: $f = \frac{[a(MoSSe) - a(MoS2)]}{a(MoS2)} = \frac{\frac{1}{OG_2} - \frac{1}{OG_1}}{\frac{1}{OG_1}} * 100\% = 0.8\,\%$ **e,** Low-magnification STEM image of $MoS_2$-MoSSe heterostructure. **f,** The corresponding Fourier transform in **(e)**. x and y represent the two Bragg reflections to calculate strain mapping. **g-h,** $\varepsilon_{xx}$ and $\varepsilon_{yy}$ represent the strain mappings along x and y directions, respectively.

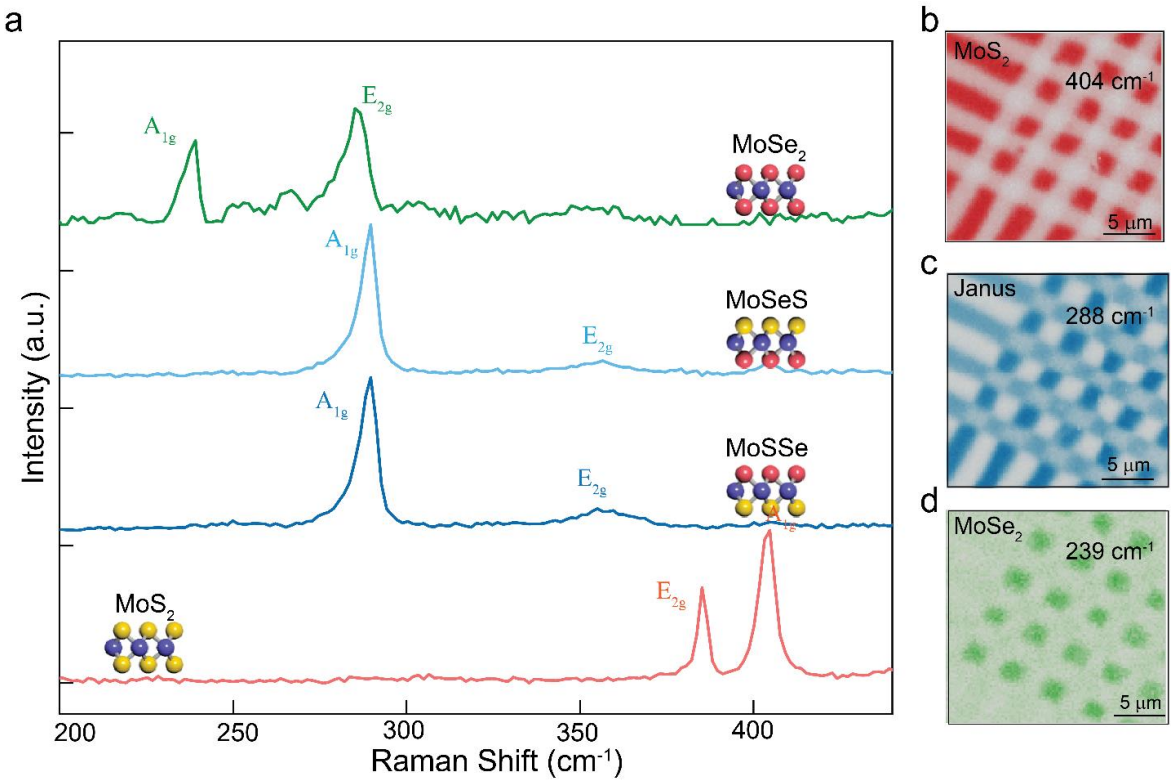


**Figure S8. Morphology and spectroscopy characterizations for the lateral multi-heterostructure based on monolayer $MoS_2$-Janus MoSSe-Janus MoSeS-$MoSe_2$. a,** Raman spectra of individual monolayer $MoS_2$, Janus MoSSe, Janus MoSeS and $MoSe_2$ regions in the multi-heterostructure. **b-d,** Spatial resolved Raman mappings for the $A_{1g}$ mode of monolayer $MoS_2$, Janus MoSSe (or MoSeS) and $MoSe_2$ patterns, respectively.

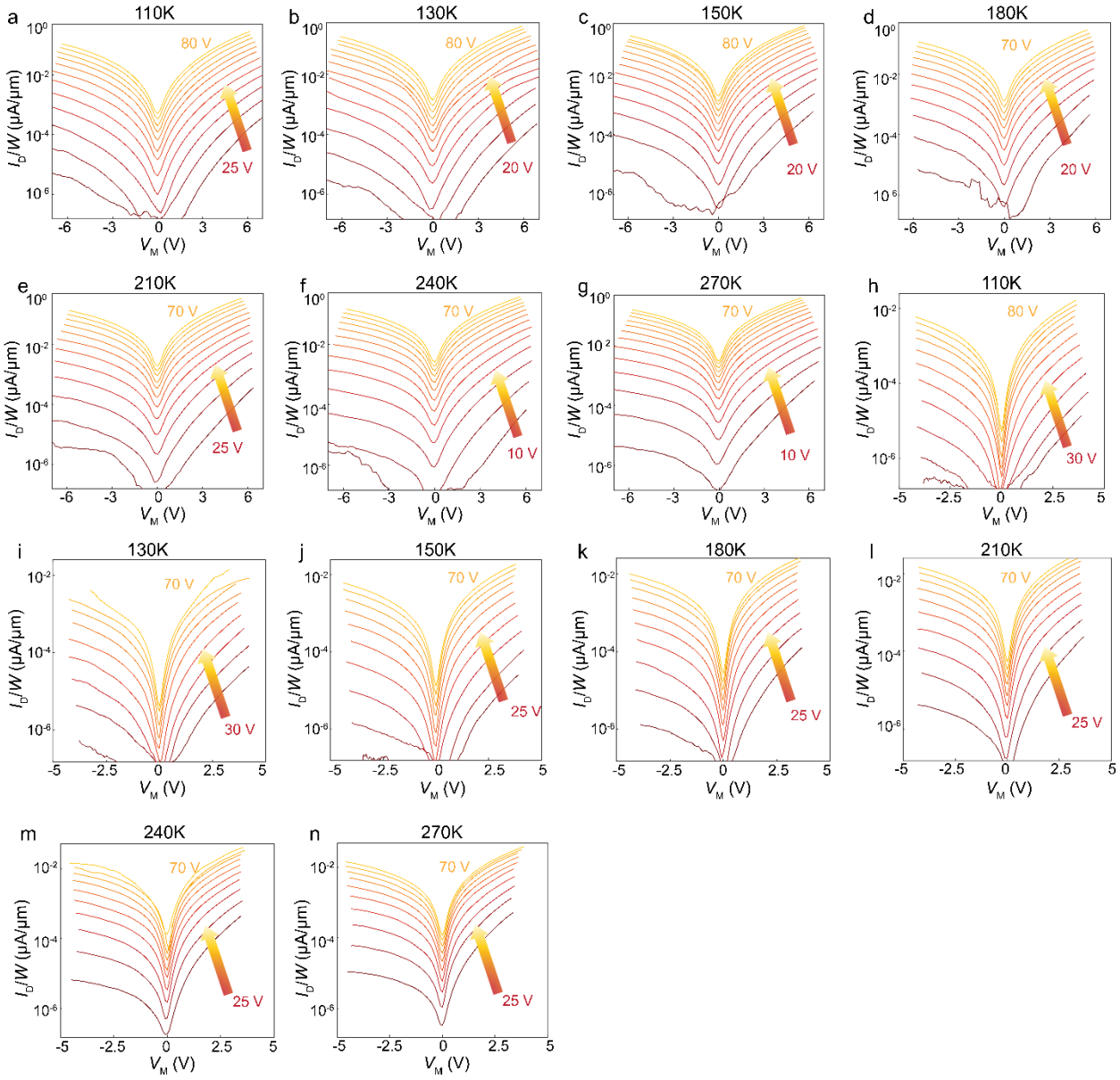


**Figure S9. a-g,** Output characteristics of the MoSSe-$MoS_2$ lateral heterojunction with various temperatures. **a,** 110 K. **b,** 130 K. **c,** 150 K. **d,** 180 K. **e,** 210 K. **f,** 240 K. **g,** 270 K. **h-n,** Output characteristics of the $MoSe_2$-MoSeS lateral heterojunction with various temperatures. **h,** 110 K. **i,** 130 K. **j,** 150 K. **k,** 180 K. **l,** 210 K. **m,** 240 K. **n,** 270 K.

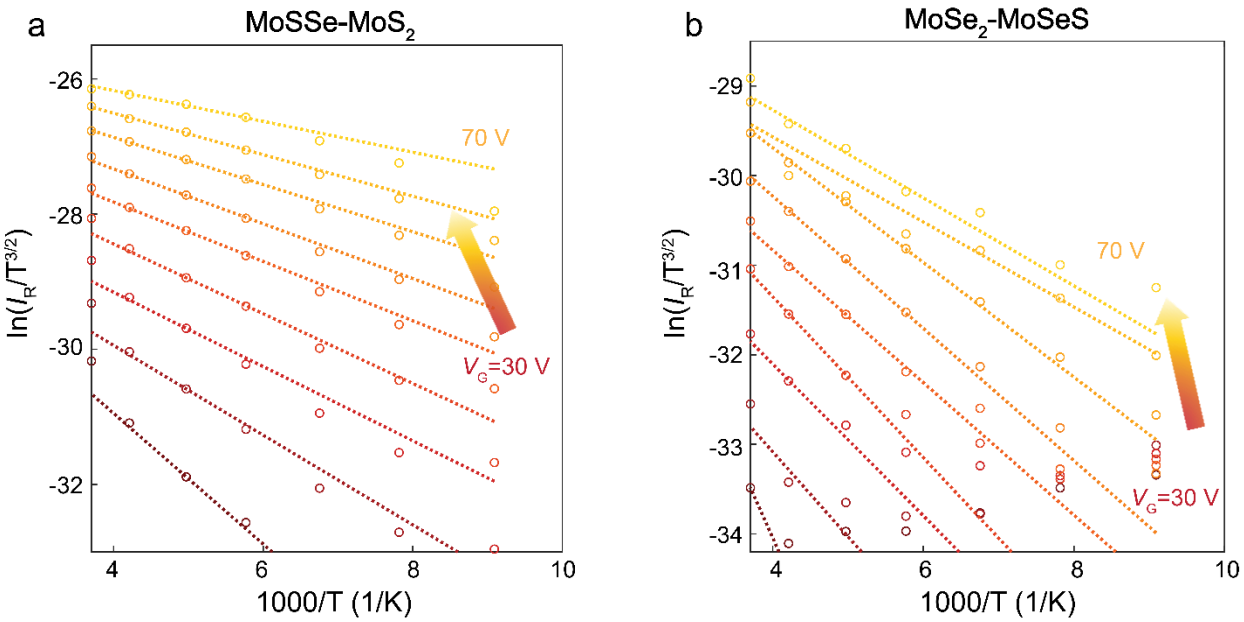


**Figure S10.** Arrhenius plots of: **a**, $MoSSe\text{-}MoS_2$ lateral heterojunction. **b**, $MoSe_2$-MoSeS lateral heterojunction.

## References


1. Hÿtch, M., Snoeck, E. & Kilaas, R. Quantitative measurement of displacement and strain fields from HREM micrographs. *Ultramicroscopy* **74**, 131-146 (1998).
2. Ling, X. *et al.* Parallel Stitching of 2D Materials. *Adv. Mater.* **28**, 2322-2329 (2016).
3. Giannozzi, P. *et al.* QUANTUM ESPRESSO: a modular and open-source software project for quantum simulations of materials. *J. Phys-Condens. Mat.***21**, 395502 (2009).
4. J. Heyd, G. E. Scuseria, and M. Ernzerhof. Hybrid functionals based on a screened Coulomb potential. *J. Chem. Phys.* **118**, 8207 (2003).
5. Xie, K. C., Li, X. S. & Cao, T. Theory and Ab Initio Calculation of Optically Excited States-Recent Advances in 2D Materials. *Adv. Mater.* 1904306 (2019).